

# High-Temperature Erosive Behavior of Plasma Sprayed Cr<sub>3</sub>C<sub>2</sub>-NiCr/Cenosphere Coating

Mahantayya Mathapati, Mrityunjay Doddamani, and M.R. Ramesh

(Submitted June 8, 2017; in revised form December 29, 2017; published online February 23, 2018)

This research examines the deposition of Cr<sub>3</sub>C<sub>2</sub>-NiCr/cenosphere and Cr<sub>3</sub>C<sub>2</sub>-NiCr coatings on MDN 321 steel through the process of plasma spray. In this process, the solid particle erosion test is established at 200, 400, 600 °C with 30° and 90° impact angles. Alumina erodent is adopted to investigate the erosive behavior of the coating at higher temperatures. The properties of the Cr<sub>3</sub>C<sub>2</sub>-NiCr/cenosphere coating are established based on the microhardness, the adhesive strength, the fracture toughness, and the ductility. To quantify volume loss as a result of erosion, an optical profilometer is used. At higher temperature, decrease in the erosion volume loss of Cr<sub>3</sub>C<sub>2</sub>-NiCr/cenosphere and Cr<sub>3</sub>C<sub>2</sub>-NiCr coatings is observed. The erosion-resistive property of Cr<sub>3</sub>C<sub>2</sub>-NiCr/cenosphere coating is higher than that of MDN 321 steel by 76%. This property is influenced by high-temperature stability of mullite, alumina, and protective oxide layer that is formed at elevated temperatures. The morphology of eroded coating discloses a brittle mode of material removal.

**Keywords** brittle failure, cenospheres, erosion, plasma spray

## 1. Introduction

The impingement of particle on the surface of a target in the process of material removal is referred to as erosion. The impingement becomes critical at elevated temperatures in applications like gas and steam turbines, rotor blades of jet engine, boiler tubes in coal-fired power plant, etc. (Ref 1). Service states of such components in high-temperature environments may trade off their mechanical properties bringing about lessened life cycle. Reasonable surface alteration methods, for example, plasma sprayed cermet coatings (Ref 2) upgrade erosive protection for such applications. Cr<sub>3</sub>C<sub>2</sub>-NiCr coatings are normally utilized as a part of high-temperature erosion, wear and corrosion resistive applications. Carbide particles embedded in NiCr matrix impart high hardness and strength to coatings up to 900 °C (Ref 3-5). Further, coefficient of thermal expansion of Cr<sub>3</sub>C<sub>2</sub> ( $10.3 \times 10^{-6} \text{ }^\circ\text{C}^{-1}$ ) is closer to iron ( $11.4 \times 10^{-6} \text{ }^\circ\text{C}^{-1}$ ) and Ni ( $12.8 \times 10^{-6} \text{ }^\circ\text{C}^{-1}$ ), which are the base alloys for high-temperature applications. Such a composition if chosen, thermal mismatch in high-temperature environment can be minimized to a great extent. In addition at high temperatures, protective oxide layer formed on the coating surface provides resistance to erosion (Ref 6). However, Cr<sub>3</sub>C<sub>2</sub>-NiCr in powder form is quite expensive limiting wide adaptability in different structural components. This necessitates finding inexpensive solutions and probable alternative in developing coatings based on industrial wastes like fly ash cenospheres.

Fly ash is a richly accessible industrial waste, generated because of combustion of coal in thermal power plants. These fly ash cenospheres are spherical in shape, economical, and readily available in powder form and possess superior mechanical properties. They contain mostly oxides of silicon (SiO<sub>2</sub>), aluminum (Al<sub>2</sub>O<sub>3</sub>), iron (Fe<sub>2</sub>O<sub>3</sub>), and mullite (3Al<sub>2</sub>O<sub>3</sub>·2SiO<sub>2</sub>). Among them, aluminum oxide and mullite have high-temperature stability, wear, erosion, and corrosion resistance (Ref 7-9), which can be exploited as proposed in the present work. Mishra et al. (Ref 10) proposed suitability of fly ash coating using plasma spray technique. Hardness and sliding wear behavior of fly ash coating deposited using detonation spray technique on mild steel is studied by Rama Krishna et al. (Ref 11). Their investigation uncovers that fly ash coating has better hardness and coefficient of friction than mild steel. Sidhu et al. (Ref 12) investigated wear, oxidation, and salt corrosion behavior of plasma sprayed fly ash coating. Their study reveals that coating exhibits better oxidation and salt corrosion resistance than carbon steel substrate. Sahu et al. (Ref 13) reported erosive behavior of plasma sprayed fly ash premixed with aluminum and noted increasing erosion resistance with aluminum addition. Behera and Mishra (Ref 14) studied plasma sprayed fly ash composite coating mixed with quartz and ilmenite on copper substrate and observed that adhesion strength of composite coating increased with increase in plasma torch input level. Sunil et al. (Ref 15) studied effect of process parameters on the mechanical properties of plasma sprayed TiO<sub>2</sub> and fly ash composite coating. They reported that current density influences on the mechanical properties of the coating. Not very many examinations are accessible in later part on utilization of fly ash coatings. Be that as it may, these examinations did not address erosive behavior at elevated temperatures calls for investigation of Cr<sub>3</sub>C<sub>2</sub>-NiCr/fly ash cenosphere coating. Utilization of such environmental pollutants in coatings may additionally decrease landfill burden if developed successfully and can be dealt with as a eco-accommodating coatings.

The present work deals with MDN 321 steel substrate, which is most ordinarily utilized for jet engine parts, expansion

Mahantayya Mathapati, Mrityunjay Doddamani, and M.R. Ramesh, Department of Mechanical Engineering, National Institute of Technology Karnataka, Surathkal, India. Contact e-mail: mahantkm.me14f09@nitk.edu.in.

joints, exhaust manifolds, chemical production equipments in high-temperature environments and fire tube boilers (Ref 16).  $\text{Cr}_3\text{C}_2\text{-NiCr}$ /fly ash cenosphere and  $\text{Cr}_3\text{C}_2\text{-NiCr}$  coatings are deposited on MDN 321 steel substrate using atmospheric plasma spray process. The erosion behavior of coatings and substrate is investigated at 200, 400, 600 °C with 30° and 90° impingement angles using  $\text{Al}_2\text{O}_3$  erodent. Weight and volume loss methods are used to estimate erosion loss. Erosion mechanism of coating and substrate is dealt elaborately with scanning electron microscopy (SEM) and energy dispersive spectroscopy (EDS).

## 2. Materials and Methods

### 2.1 Materials

MDN 321 steel procured from Mishra Dhatu Nigam Ltd., Hyderabad, India, is utilized as substrate, and its chemical composition (wt.%) is 0.10 C, 1.46 Mn, 18.13 Cr, 10.36 Ni, 0.62 Ti, 0.55 Si, and balance Fe. Substrate is trimmed to the dimension of  $25 \times 20 \times 4$  mm using diamond saw prior to the plasma spraying. Commercially available agglomerated and sintered  $\text{Cr}_3\text{C}_2\text{-25NiCr}$  powder (M/s. Spraymet Surface Technologies Pvt. Ltd., Bangalore, India) and fly ash cenospheres (Cenospheres India Pvt. Ltd., Kolkata, India) are used as coating feedstock. Mean particle diameter and density of  $\text{Cr}_3\text{C}_2\text{-25NiCr}$  powder are noted to be 50  $\mu\text{m}$  (laser diffraction technique using Cilas 1064, France) and 2.6  $\text{g/cm}^3$ , respectively. Mean particle diameter and density of cenospheres are 65  $\mu\text{m}$  and 0.85  $\text{g/cm}^3$ , respectively (Ref 17-21). These powders are blended mechanically having 70% mass fraction of  $\text{Cr}_3\text{C}_2\text{-25NiCr}$  with 30% fly ash cenospheres. Figure 1 presents SEM micrograph of blended feedstock. Uniform dispersion of cenospheres in  $\text{Cr}_3\text{C}_2\text{-NiCr}$  is apparent from the micrograph. Further, cenospheres are seen to be intact, i.e., without any breakage due to mechanical blending.

### 2.2 Coating Deposition and Characterization

Plasma spraying of  $\text{Cr}_3\text{C}_2\text{-NiCr}$ /cenospheres blend and  $\text{Cr}_3\text{C}_2\text{-NiCr}$  is carried out using METCO USA 3 MB. The erosion performance of  $\text{Cr}_3\text{C}_2\text{-NiCr}$ /cenosphere coating is compared with  $\text{Cr}_3\text{C}_2\text{-NiCr}$  coating. Adhesion between the coating and substrate is ensured by grit blasting the surface of substrate before being plasma sprayed using alumina powder

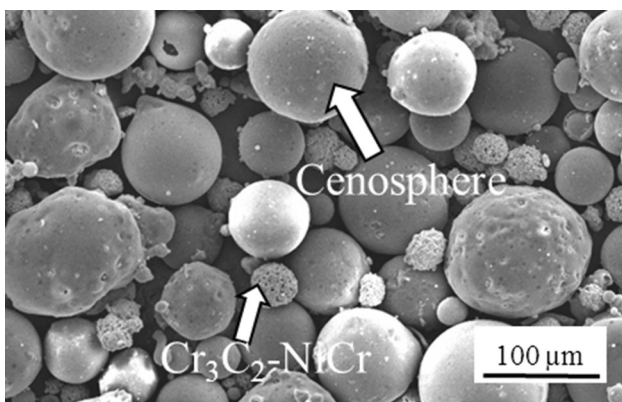


Fig. 1 Morphology of as-blended  $\text{Cr}_3\text{C}_2\text{-NiCr}$  and cenospheres

(mean particle dia. of 150  $\mu\text{m}$ ). Table 1 lists spray parameters used in the plasma spray process. Amid plasma spraying, powder is supplied by the feeder, which is mixed with argon gas at predetermined pressure. Further, mixture flows towards the plasma stream prior to getting deposited on the substrate. Deposition of coating per pass is in the range of 12-15  $\mu\text{m}$  with 40-45% spraying efficiency. The phases present in blended powder and coating are analyzed by x-ray diffraction (XRD) (DX GE-2P, JEOL, JAPAN). Coated samples are sectioned using diamond saw for micrographic analysis. Samples are polished along the cross section using 220, 400, 600, 800, 1000 grit emery papers followed by 1/0, 2/0, 3/0, and 4/0 grade emery papers. Final mirror finish is obtained by cloth polishing using 0.5  $\mu\text{m}$  diamond paste. Cross-sectional microstructure is observed through SEM. Porosity of the coating is computed using optical microscope supported with biovis image analyzer (ARTRAY, AT 130, JAPAN). Twenty view fields are analyzed, and average values are reported. Microhardness is measured on the cross section of the coating and substrate at 300 g load using OMNITECH Vickers microhardness tester. Average values are reported from 20 indentations taken at different locations.

### 2.3 Ductility

Ductility of the thermal sprayed cermet coatings differs from bulk materials (Ref 22). Nano-indentation test is carried out on the binder and hard phase using nano-hardness tester (Agilent, G200, USA). Ductility of the coating is measured by load-

Table 1 Plasma spray process parameters

Plasma gas (argon + hydrogen)	Pressure	0.75 MPa
	Flow rate	40 lpm
Powder carrier gas (Argon)	Pressure	0.35 MPa
	Flow rate	7 lpm
Current		490 A
Voltage		60 V
Powder feed rate		60 g/min
Stand of distance		100-125 mm

As provided by Spraymet Surface Technology Pvt. Ltd., Bangalore, India

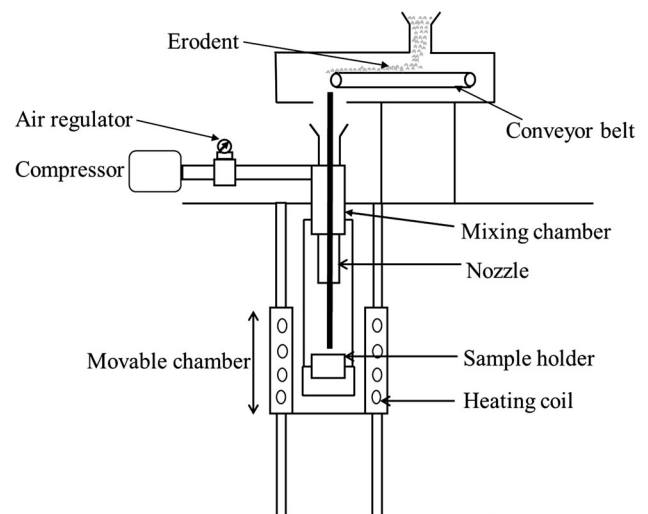


Fig. 2 Schematic representation of the erosion test setup

displacement plots obtained from nano-indentation test using ratio of the plastic work,  $W_p$  to total work,  $W_t$  (Ref 23).  $W_p$  is estimated from the area enclosed by the loading–unloading curve, and  $W_t$  is represented by the area below loading curve in load–displacement plot.

## 2.4 Adhesion Strength and Indentation Fracture Toughness

The adhesion strength of the coating is assessed utilizing ASTM C-633-13 (pull-off method) standard. Test is carried out in tension mode using universal testing machine (AG–X plus, Shimadzu hydraulic tensile test machine, Japan) with strain rate of 0.016 mm/s. Cylindrical samples of dimension 25 × 25 mm are used for the adhesion strength test. HTK Ultra bond epoxy resin is utilized as glue to stick Cr<sub>3</sub>C<sub>2</sub>-NiCr/cenosphere coated sample with the counter block. Samples are cured at 150 °C for 3 h in tubular furnace preceding test (Heatron Industrial Heaters, Mangalore, India). The adhesion strength is estimated

by evaluating the ratio of maximum tensile load to cross-sectional area, and average values of five samples are reported.

Fracture toughness of the coating is calculated by indentation method. Indentation is carried out with 1 kg load using Vickers pyramid indenter, wherein the diagonal of indenter is parallel to coating–substrate interface. Equation for fracture toughness using crack length is given by Ref 16,

$$K_{IC} = 0.0193(H_V d)(E/H_V)^{2/5}(a)^{-1/2} \dots (c/d \leq 2.5)$$

Palmqvist Cracks (Eq 1)

$$K_{IC} = 0.0711(H_V d^{1/2})(E/H_V)^{2/5}(c/d)^{-3/2} \dots (c/d \geq 2.5)$$

Half penny Cracks (Eq 2)

where ' $H_V$ ' is the Vickers hardness, ' $E$ ' is the Young's modulus, and ' $d$ ' is the half diagonal of the Vickers indentation. The radial crack length ' $a$ ' equals difference between indentation crack length ' $c$ ' and half diagonal of the Vickers indentation ' $d$ '. Values of ' $a$ ', ' $c$ ', and ' $d$ ' are measured from SEM micrographs.

**Table 2 Erosion test parameters**

Erodent	Alumina
Erodent average size, $\mu\text{m}$	50
Erodent velocity, m/s	30
Erodent feed rate, g/min	2
Impact angle, °	30 and 90
Temperature, °	200, 400 and 600
Test time, min	15
Standoff distance, mm	10
Nozzle diameter, mm	1.5

## 2.5 Erosion Test

Solid particle erosion test is carried out on both coated samples and substrates as per ASTM G76-13 standard using air jet erosion tester (TR-471-800, Ducom instruments private limited, Bangalore, INDIA). Alumina grit is utilized as erodent. Schematic representation of the test setup is presented in Fig. 2. Erodent is fed into mixing chamber using conveyor belt at 2 g/min to get mixed with heated air flowing through spiral tube which in turn is surrounded by tubular heaters. Erodent and air

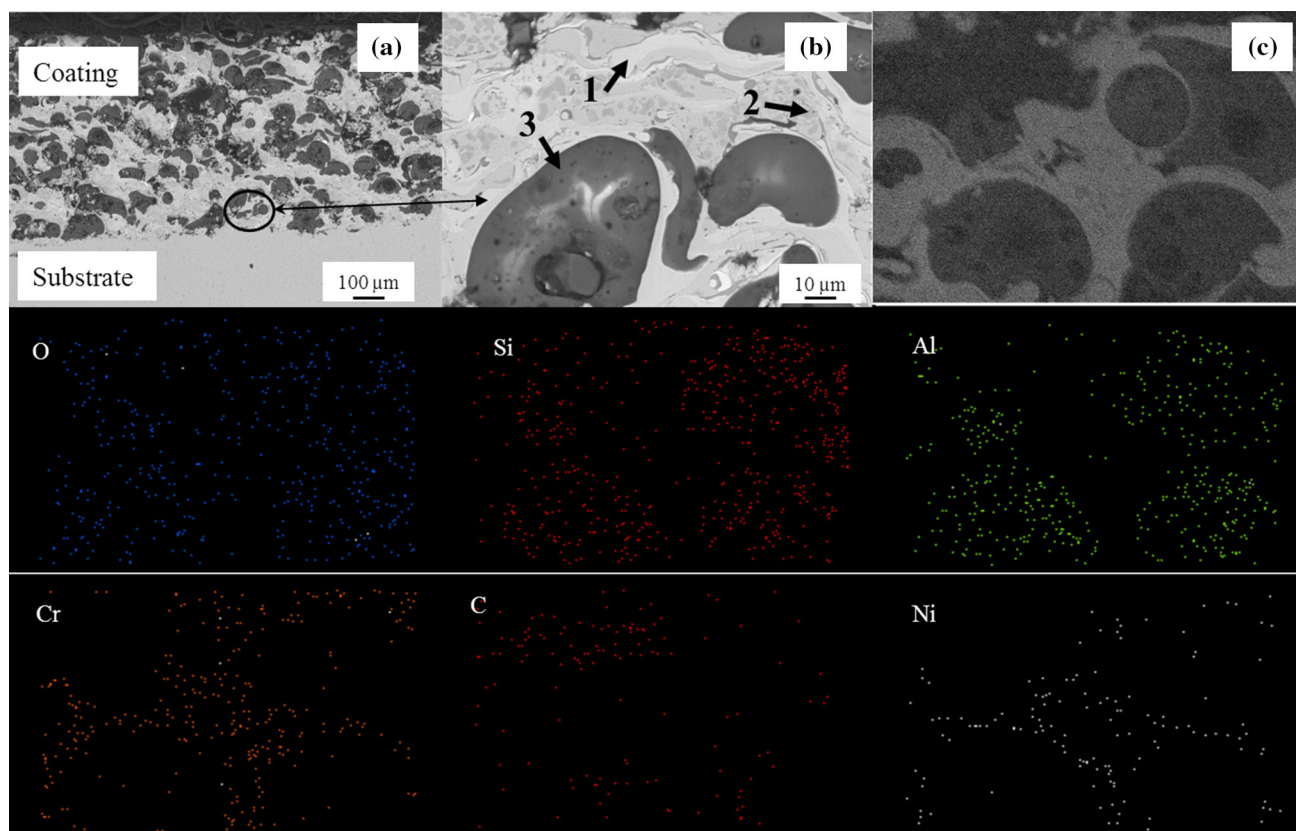


**Fig. 3** (a) and (b) Micrographs of as-deposited Cr<sub>3</sub>C<sub>2</sub>-NiCr/cenosphere coating and (c) EDS elemental mapping

mixture impinge at 30 m/s on the sample, which is rigidly fixed in the holder as shown in Fig. 2. Eroderent velocity is measured by double disc method prior to the test. Specimen kept in sample holder is heated by bottom heater comprising of hollow cylinder with heating elements. Impact angle on specimen is varied by changing sample holder orientation with respect to the particle stream flowing out of the nozzle. Table 2 presents erosion test parameters used in the present work.

Preceding the test, samples are cleaned in acetone, dried, and clamped in the erosion testing machine. All the samples are subjected to the predefined temperatures for 20 min before test to reproduce actual testing conditions. Samples after test are acetone cleaned, dried, and weighed using electronic weighing balance (least count of 0.0001 g) to estimate mass loss. The erosion rate is computed by ratio of mass loss to erodent particles mass. The volume loss of the eroded samples is quantified using 3-D optical non-contact profilometer (Zeta instruments, USA). Test is carried out three times for each test conditions, and average value is reported.

### 3. Results and Discussion

#### 3.1 Microstructure Analysis of Coating

Figure 3(a) presents cross-sectional micrograph of as-deposited  $\text{Cr}_3\text{C}_2$ -NiCr/cenosphere coating. As observed from the

**Table 3** EDS analysis of coating at the designated point in Fig. 3(b)

Element	Oxide	Phase 1	Phase 2	Phase 3
...	$\text{SiO}_2$	...	...	60.70
...	$\text{Al}_2\text{O}_3$	...	...	36.24
...	$\text{Fe}_2\text{O}_3$	...	...	3.04
C	...	04.39	14.05	...
Cr	...	19.27	60.84	...
Ni	...	74.67	25.11	...

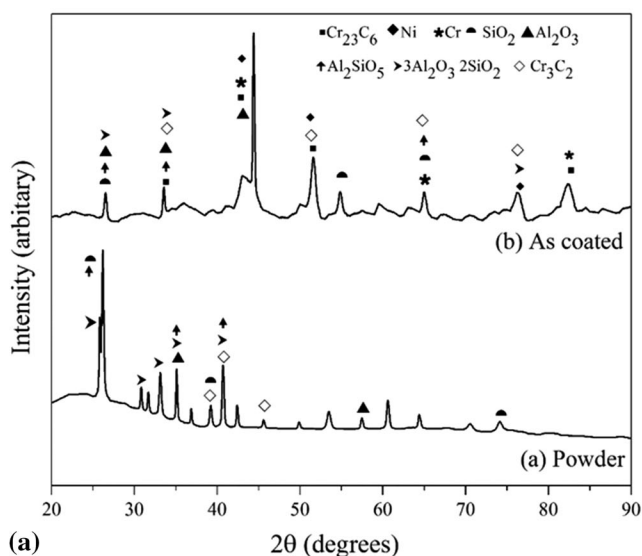
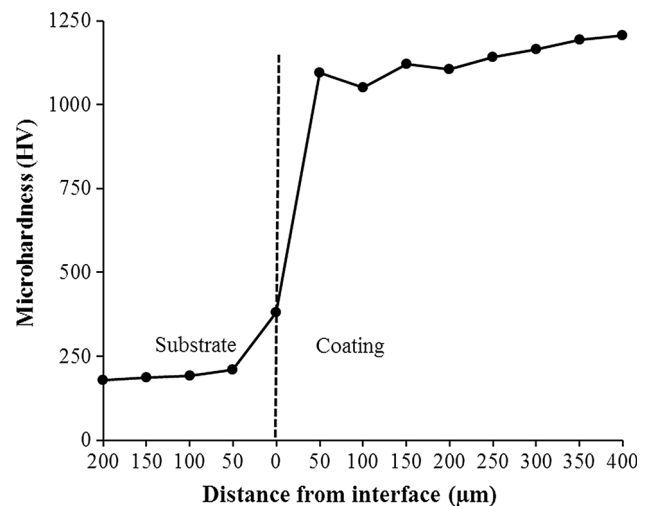


**Fig. 4** (a) XRD pattern of as-blended powder and  $\text{Cr}_3\text{C}_2$ -NiCr/cenosphere coated sample (b) eroded sample at different temperatures

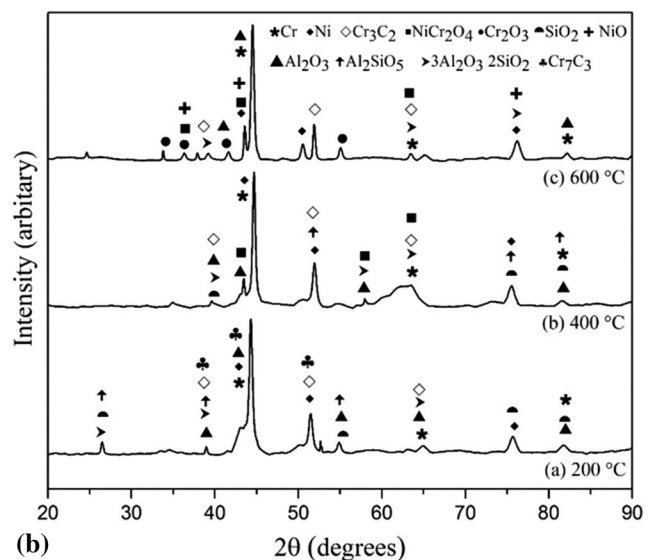
micrograph, coating is bonded well with substrate and shows uniform dispersion of the cenospheres. Average thickness of coating observed is  $400\ \mu\text{m}$  with an average area porosity of  $3.5 \pm 0.5\%$ . Micrograph of marked zone in Fig. 3(a) is presented in Fig. 3(b). Lamellar dense packed structure of  $\text{Cr}_3\text{C}_2$ -NiCr is evident from Fig. 3(b). Constituents of the coating are identified based on EDS analysis (Table 3) and present are marked as 1-NiCr solid solution matrix, 2- $\text{Cr}_3\text{C}_2$  particles embedded in NiCr matrix, and 3-cenosphere particles. Figure 3(c) depicts elemental mapping of coating, which clearly shows distinct splats enriched with oxygen and coexists with silicon and aluminum indicating the presence of respective oxides on the cenospheres. Nickel and chromium are distributed around the cenospheres splats uniformly.

#### 3.2 XRD Analysis

The x-ray diffraction pattern of blended powder and as-sprayed  $\text{Cr}_3\text{C}_2$ -NiCr/cenosphere coating is presented in



**Fig. 5** Microhardness profile of substrate and  $\text{Cr}_3\text{C}_2$ -NiCr/cenosphere coating





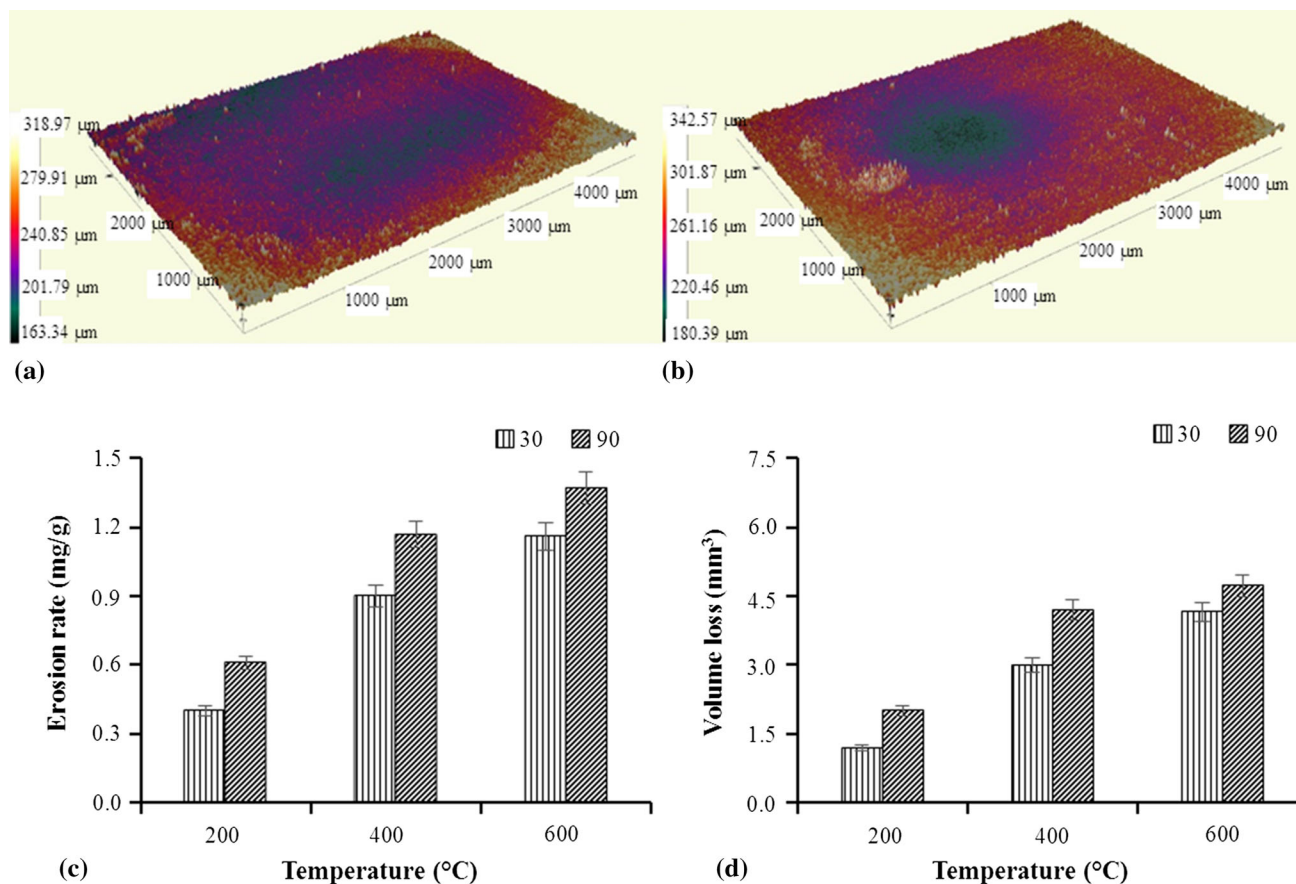


**Fig. 6** (a) and (b) Eroded profiles of substrate at 600 °C, (c) erosion rate, and (d) volume loss as function of temperature at 30° and 90° impact angles, respectively

Fig. 4(a). Distinct major peaks of  $3\text{Al}_2\text{O}_3\cdot 2\text{SiO}_2$ ,  $\text{Al}_2\text{SiO}_5$ , and  $\text{SiO}_2$  and minor peaks of  $\text{Cr}_3\text{C}_2$ ,  $\text{Al}_2\text{O}_3$  are observed in blended powder. The slight broadened peaks are observed in the coated samples due to differential dissolution of carbides in NiCr binder.  $\text{Cr}_{23}\text{C}_6$ , Cr, and Ni are major peaks while  $\text{SiO}_2$ ,  $\text{Al}_2\text{SiO}_5$  are minor peaks in the coated sample as observed from Fig. 4(a). The x-ray diffraction pattern of eroded samples at 200, 400, and 600 °C is presented in Fig. 4(b). Considerable difference in intensity is not seen at highest intensity peaks at 200, 400, and 600 °C, and intensity is observed to be 800 arbitrary unit. There is no evidence of oxide formation at 200 °C. Nevertheless, at elevated temperatures, oxides of active elements of coating are seen to be formed.  $\text{NiCr}_2\text{O}_4$  is observed to be formed at 400 °C, whereas the presence of  $\text{Cr}_2\text{O}_3$ ,  $\text{NiCr}_2\text{O}_4$ ,  $\text{NiCrO}_3$ , and  $\text{NiO}$  is observed at 600 °C.

### 3.3 Microhardness Measurement

The variation in microhardness values as a function of distance from the coating–substrate interface is shown in Fig. 5. The average microhardness of the coating and the substrate is  $1134 \pm 52$  and  $189 \pm 10$  HV, respectively. Microhardness is increased across the interface of substrate and coating due to peening stresses developed during grit blasting prior to coating process. This results in work hardening of substrate. Microhardness of the coating is seen to be varied along the cross section due to in homogenities in the coating microstructure.

### 3.4 Ductility

Ductility of the  $\text{Cr}_3\text{C}_2$ -NiCr/cenosphere coating is measured in binder and hard phases.  $W_p/W_t$  varies between 0 (perfectly elastic) and 1 (perfectly plastic) (Ref 23).  $W_p/W_t$  ratio of the coating in the binder and hard phases is 0.86 and 0.57, respectively, indicating better ductility. Further, it represents plastic deformation of the matrix preferred for improving coating erosion resistance.

### 3.5 Adhesion Strength and Indentation Fracture Toughness

Durability of the coatings depends on adhesion strength between the substrate and coating. Fracture surface reveals adhesive failure between  $\text{Cr}_3\text{C}_2$ -NiCr/cenosphere coating and substrate interface. The adhesion strength of the coating is  $10.60 \pm 2$  MPa. Comparative estimations of adhesion strength are accounted for by Behera and Mishra (Ref 14) and Mishra et al. (Ref 24) for the plasma sprayed fly ash-based composite coatings. Fracture toughness is computed using Eq 1 as the ratio  $c/d$  measured by indentation is in the range of 1-1.6 indicating existence of Palmqvist cracks. Cracks are initiated from the indenter end and are parallel to the coating–substrate interface. The average value of fracture toughness observed is  $5.4 \pm 0.40$  MPa  $\text{m}^{1/2}$ , which is higher than fracture toughness revealed by Robertson and White (Ref 25) and Bolelli et al. (Ref 26) for  $\text{Cr}_3\text{C}_2$ -NiCr HVOF sprayed coatings.

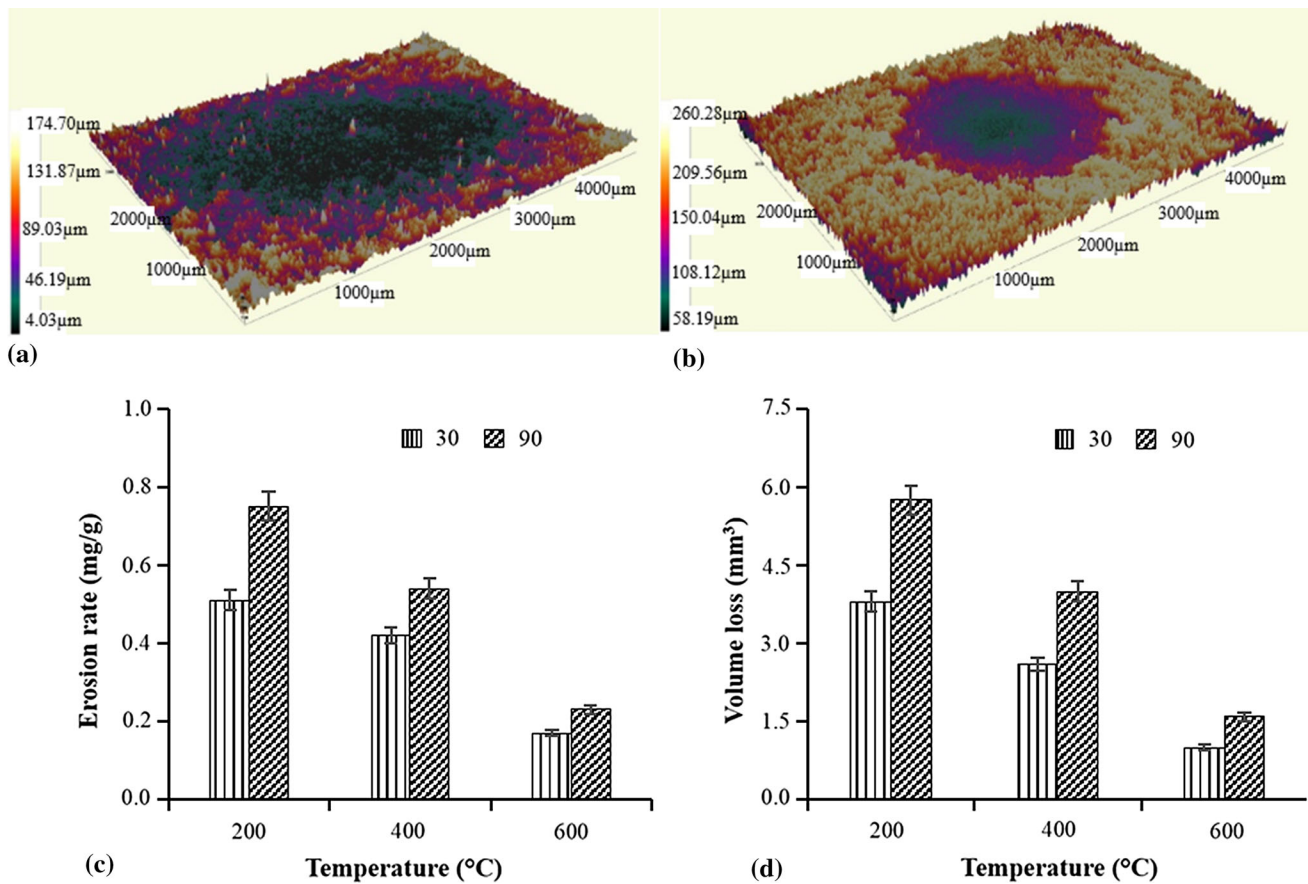


**Fig. 7** (a) and (b) Eroded profiles of Cr<sub>3</sub>C<sub>2</sub>-NiCr/cenosphere coating at 600 °C, (c) erosion rate, and (d) volume loss as function of temperature at 30 and 90° impact angles, respectively

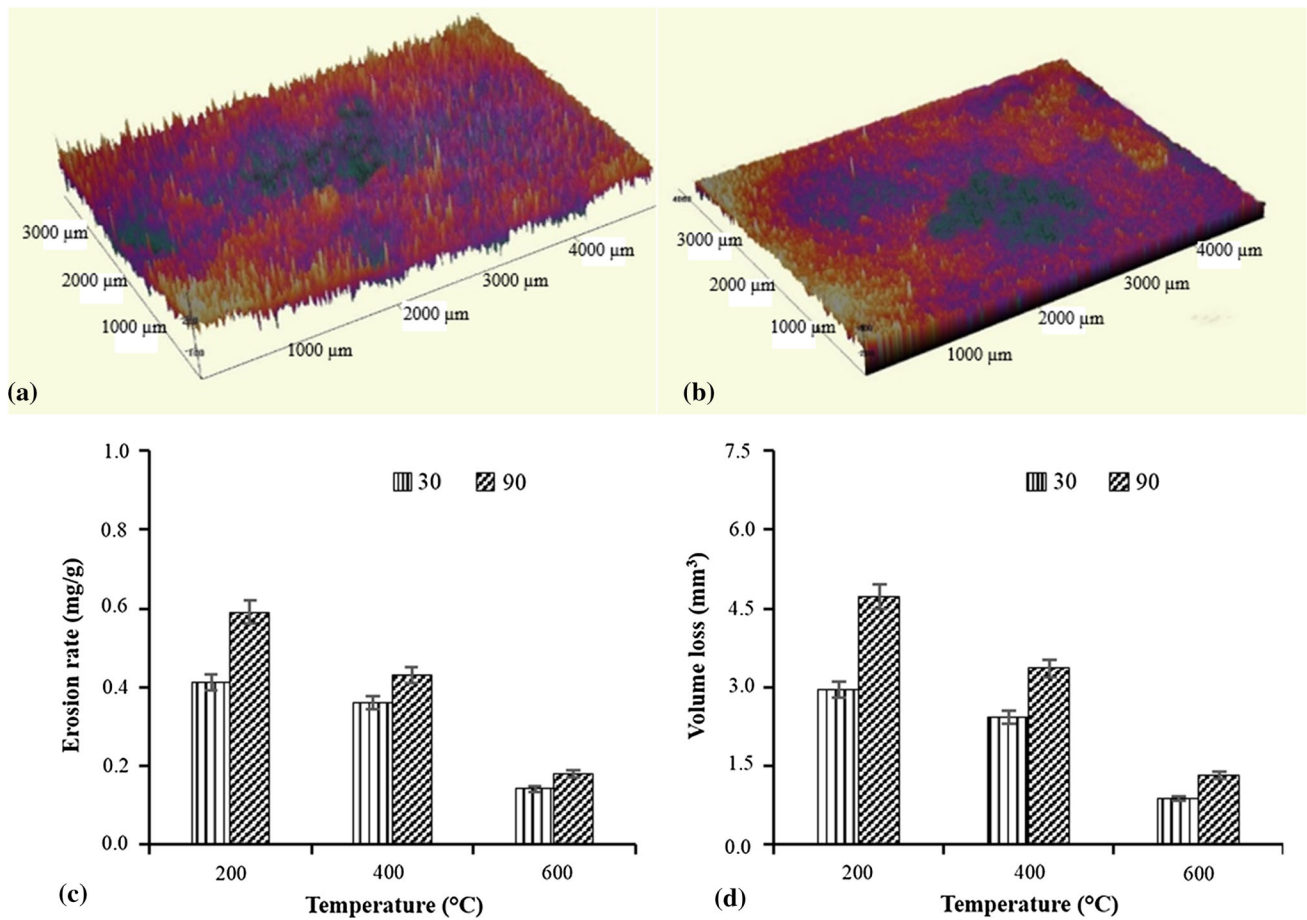
### 3.6 Erosive Behavior of Substrate and Coating

Figure 6(a) and (b) presents 3-D profiles of eroded substrate surface at 600 °C with impact angles of 30 and 90°, respectively. Large crater is observed at 90° impact angle as seen in Fig. 6(b), which demonstrates maximum material expulsion brought about higher erosion volume loss. Effect of temperature on the erosion rate and volume loss is presented in Fig. 6(c) and (d). Erosion rate and volume loss increase with increase in the test temperature and impact angle, more conspicuous being at higher values (Fig. 6c and d). Erosion volume loss at 600 °C is approximately 3.5 and 2.5 times higher than at 200 °C for 30° and 90° impact angles, respectively. Increment in the test temperature brings about abatement of substrate hardness owing to annealing effect. At higher temperatures, formed oxide layer is lacking to oppose erodent impact bringing about oxide layer splitting and its consequent evacuation. Consequently increasing volume loss is noted with ascend in test temperature.

Three-dimensional profiles of eroded Cr<sub>3</sub>C<sub>2</sub>-NiCr/cenosphere coating surface at 600 °C with 30 and 90° impact angles are presented in Fig. 7(a) and (b). Material is removed in larger area at 30° impact angle (Fig. 7a) indicates erodent particle slides at first glance amid the erosion test where in at 90° impact angle material is expelled in smaller area with more profundity of the holes shows erodent impinging the surface without sliding at first glance. Effect of temperature on the erosion rate and volume loss is presented in Fig. 7(c) and (d). It is observed that the erosion rate and volume loss of the coating

diminish with increment in temperature for both the impact angles and are lower at 30°. Comparable outcomes are accounted for by Yang et al. (Ref 3) for Cr<sub>3</sub>C<sub>2</sub>-NiCr coating for boiler tube application. The erosion volume loss at 600 °C is noted to be four times less than that observed at 200 °C. The decline in the erosion volume loss with temperature rise is credited to higher hardness and temperature stability of the constituents present in the coating. At higher temperature, ductility of the coating increases, prompting plastic deformation of NiCr binder phase. This reduces the localized brittle cracking of binder phase and hard particles interface (Ref 27). In addition, protective oxide layer of Cr<sub>2</sub>O<sub>3</sub>, NiCr<sub>2</sub>O<sub>4</sub>, and NiO has been formed at higher temperatures reducing further coating volume loss. The erosion volume loss at 90° impact angle is more than that at 30° at all the test temperatures, inferring brittle mode of material removal. At 90° impact angle, the region of contact is less for erodent particles and because of strain localization, oxide layer fails to resist impact load by formations of fragments, leading to cracks. Accordingly, erosion volume loss is apparently increased.

Figure 8(a) and (b) presents 3-D profiles of eroded Cr<sub>3</sub>C<sub>2</sub>-NiCr coating surface at 600 °C with impact angles of 30 and 90°, respectively. Contact area of erodent during testing at 30° impact angle is more as compared to 90° impact angle. Effect of temperature on the erosion rate and volume loss is presented in Fig. 8(c) and (d). Cr<sub>3</sub>C<sub>2</sub>-NiCr coating displays comparable erosion rate and volume loss slant trend as that of Cr<sub>3</sub>C<sub>2</sub>-NiCr/cenospheres coating. Erosion rate and volume loss of



**Fig. 8** (a) and (b) Eroded profiles of  $\text{Cr}_3\text{C}_2\text{-NiCr}$  coating at 600 °C, (c) erosion rate, and (d) volume loss as function of temperature at 30 and 90° impact angles, respectively

$\text{Cr}_3\text{C}_2\text{-NiCr}$  coating are brought down and contrasted with  $\text{Cr}_3\text{C}_2\text{-NiCr/cenosphere}$  coating at all the test temperatures. Erosion volume loss of  $\text{Cr}_3\text{C}_2\text{-NiCr}$  coating at 30° impact angle, 200 and 600 °C is 2.95 and 0.87 mm<sup>3</sup>, which are 22 and 13% lower contrasted with  $\text{Cr}_3\text{C}_2\text{-NiCr/cenospheres}$  coating, respectively. Higher erosion volume loss of  $\text{Cr}_3\text{C}_2\text{-NiCr/cenosphere}$  coating is due to the high volume fraction of cenosphere reinforcement, which leads to loose bonding between the spalts in the coating. Amid erosion test, such loosely bonded spalts are gouged out from the coating surface prompting higher erosion volume loss.

Figure 9(a) and (b) demonstrates the morphology of the eroded substrate surface at 600 °C with both the impact angles. Most extreme material loss takes place in ductile mode at low impact angles while higher impact angle represents material removal in brittle mode (Ref 28). From Fig. 9(a), it is observed that material has experienced severe plastic deformation, which brings about substrate plowing and forms lip at the exit end of the erodent. With subsequent impacts, these highly strained lips are vulnerable to get removed as micro-platelets. A few grooves and cracks are also observed in the micrograph. At higher temperature, hardness of the substrate diminishes and as the erodent particle slides, material gets deformed to get removed subsequently. At 90° impact angle (Fig. 9b), craters are observed. As erodent particles impact the surface, crack gets started bringing about oxide layer fragmentation (Fig. 9b). With consequent impact of erodent, fragments of oxide layer

are expelled from the surface in the form of micro-platelets-producing craters.

Figure 9(c) demonstrates the morphology of the eroded  $\text{Cr}_3\text{C}_2\text{-NiCr/cenosphere}$  coating surface at 600 °C under impact angle of 30°. At this lower angle, hard erodent particles slide first glance and being in contact for more extended time, form lips by plowing the binder region. With subsequent impacts, these profoundly strained lips are vulnerable to get removed as micro-platelets (Ref 29). The EDAX analysis at point '1' (plowing location) in Fig. 9(d) confirms the NiCr-rich binder phase. In addition, plowing of the relatively softer binder phase uncovered the hard particles to the erodent and further gouged out by repeated hammering impact of erodent particles leading to small craters formation.

Figure 9(e) demonstrates the morphology of eroded coating surface at 600 °C at 90°. The maximum volume loss has occurred at this angle inferring coating removal by brittle mechanism. Coating is removed by cracking and chipping owing to strain localization at higher impact angle, which is resulted in formation of craters as seen in Fig. 9(e). At first, cracks generate at the interface of matrix and hard particles as only one-third interface area is bonded together in plasma spray coatings while remaining area acts as interlamellar gaps, which can be considered as preexisting cracks (Ref 30). EDAX analysis (Fig. 9f) at point 1 confirms hard particle region, where crack is formed. With progress of erosion by erodent particles, cracks are developed and result in chipping of hard



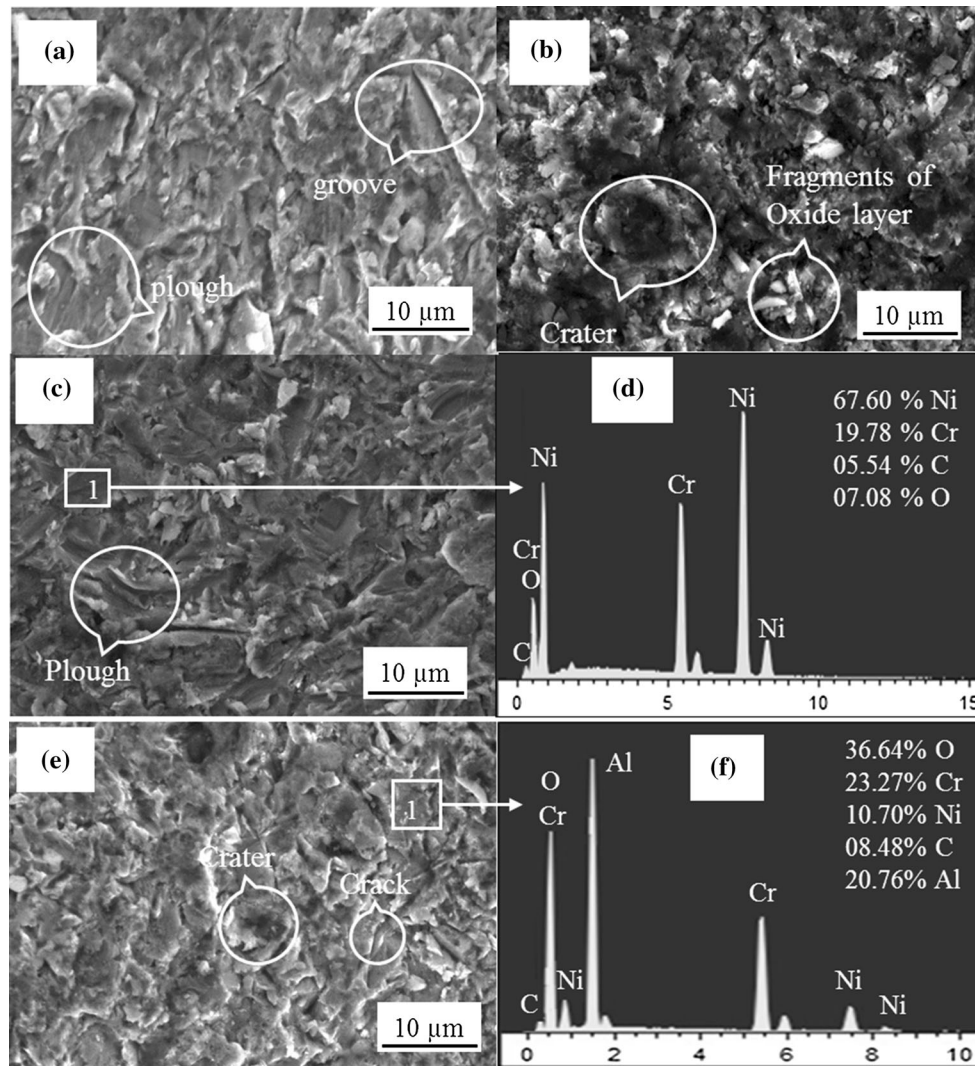


**Fig. 9** (a) and (b) SEM images of eroded surface of substrate, (c) and (e) SEM of coating, and EDAX analysis of coating at 30° and 90° impact angles in (d) and (f), respectively

particles, leading to formation of crater as observed in micrograph.

Prevailing study points out a successful development and high-temperature erosion behavior of  $\text{Cr}_3\text{C}_2\text{-NiCr}$  coating incorporating industrial waste cenosphere. The  $\text{Cr}_3\text{C}_2\text{-NiCr/cenosphere}$  coating exhibited lower erosion volume loss at elevated temperatures compared to MDN 321 steel substrate and higher erosion volume loss than  $\text{Cr}_3\text{C}_2\text{-NiCr}$  coating. Optimum percentage of cenosphere in  $\text{Cr}_3\text{C}_2\text{-NiCr}$  coating makes them suitable for high-temperature applications.

#### 4. Conclusion

- The use of plasma spray has been applied successfully in the deposition of  $\text{Cr}_3\text{C}_2\text{-NiCr/cenosphere}$  coating having adhesion strength of 10.60 MPa.
- The resistance to erosion that is developed by the  $\text{Cr}_3\text{C}_2\text{-NiCr/cenosphere}$  coating is directly proportional to the increase in temperature ranging between 200-600 °C. Erosion resistance of developed  $\text{Cr}_3\text{C}_2\text{-NiCr/cenosphere}$

coating increases with increasing temperature in the range of 200-600 °C, more prominent being at 30° impact angle. At elevated temperature, erosion resistance of coating is 76% higher than MDN 321 steel substrate.

- Higher erosion resistance of coating at elevated temperature is due to high-temperature stability of the coating constituents and formed protective oxide layer on the coating surface.
- $\text{Cr}_3\text{C}_2\text{-NiCr/cenosphere}$  coating exhibits brittle erosion mechanism, wherein material is removed by crack formation and chipping at higher impact angle.
- $\text{Cr}_3\text{C}_2\text{-NiCr}$  coating showed less erosion volume loss at 200-600 °C than  $\text{Cr}_3\text{C}_2\text{-NiCr/cenosphere}$  coating.

#### Acknowledgments

The authors are grateful to Prof. Ramesh Singh, IIT Bombay, India, for providing the optical profilometer facility. The authors wish to thank Spraymet Surface Technologies Pvt Ltd, Bangalore, India, for providing the facility of the plasma spray coating. Department



of Science and Technology grant DST/TSG/AMT/2015/394/G is acknowledged by Mrityunjay Doddamani. Authors also thank Mechanical Engineering Department of NIT-K for providing support and facilities required.

## References

1. M.R. Ramesh, S. Prakash, S.K. Nath, P.K. Sapra, and B. Venkataraman, Solid Particle Erosion of HVOF Sprayed WC-Co/NiCrFeSiB Coatings, *Wear*, 2010, **269**(3), p 197–205
2. J.K.N. Murthy and B. Venkataraman, Abrasive Wear Behaviour of WC-CoCr and Cr<sub>3</sub>C<sub>2</sub>-20 (NiCr) Deposited by HVOF and Detonation Spray Processes, *Surf. Coat. Technol.*, 2006, **200**(8), p 2642–2652
3. G.J. Yang, C.J. Li, S.J. Zhang, and C.X. Li, High-Temperature Erosion of HVOF Sprayed Cr<sub>3</sub>C<sub>2</sub>-NiCr Coating and Mild Steel for Boiler Tubes, *J. Therm. Spray Technol.*, 2008, **17**(5-6), p 782–787
4. M. Manjunatha, R.S. Kulkarni, and M. Krishna, Investigation of HVOF Thermal Sprayed Cr<sub>3</sub>C<sub>2</sub>-NiCr Cermet Carbide Coatings on Erosive Performance of AISI, 316 Molybdenum Steel, *Procedia Mater. Sci.*, 2014, **5**, p 622–629
5. J.M. Guilemany, J.M. Miguel, S. Vizcaino, C. Lorenzana, J. Delgado, and J. Sanchez, Role of Heat Treatments in the Improvement of the Sliding Wear Properties of Cr<sub>3</sub>C<sub>2</sub>-NiCr Coatings, *Surf. Coat. Technol.*, 2002, **157**(2), p 207–213
6. M. Kaur, H. Singh, and S. Prakash, High-Temperature Behavior of a High-Velocity Oxy-Fuel Sprayed Cr<sub>3</sub>C<sub>2</sub>-NiCr Coating, *Metall. Mater. Trans. A*, 2012, **43**(8), p 2979–2993
7. A. Arizmendi-Morquecho, A. Chávez-Valdez, and J. Alvarez-Quintana, High Temperature Thermal Barrier Coatings from Recycled Fly Ash Cenospheres, *Appl. Therm. Eng.*, 2012, **48**, p 117–121
8. S. Das, S. Ghosh, A. Pandit, T.K. Bandyopadhyay, A.B. Chattopadhyay, and K. Das, Processing and Characterisation of Plasma Sprayed Zirconia–Alumina–Mullite Composite Coating on a Mild-Steel Substrate, *J. Mater. Sci.*, 2005, **40**(18), p 5087–5089
9. M. Mathapati, M.R. Ramesh, and M. Doddamani, High Temperature Erosion Behavior of Plasma Sprayed NiCrAlY/WC-Co/Cenosphere Coating, *Surf. Coat. Technol.*, 2017, **325**, p p98–p106
10. S.C. Mishra, K.C. Rout, P.V.A. Padmanabhan, and B. Mills, Plasma Spray Coating of Fly Ash Pre-mixed with Aluminium Powder Deposited on Metal Substrates, *J. Mater. Process. Technol.*, 2000, **102**(1), p 9–13
11. L.R. Krishna, D. Sen, D.S. Rao, and G. Sundararajan, Coatibility and Characterization of Fly Ash Deposited on Mild Steel by Detonation Spraying, *J. Therm. Spray Technol.*, 2003, **12**(1), p 77–79
12. B.S. Sidhu, H. Singh, D. Puri, and S. Prakash, Wear and Oxidation Behaviour of Shrouded Plasma Sprayed Fly Ash Coatings, *Tribol. Int.*, 2007, **40**(5), p 800–808
13. S.P. Sahu, A. Satapathy, A. Patnaik, K.P. Sreekumar, and P.V. Ananthapadmanabhan, Development, Characterization and Erosion Wear Response of Plasma Sprayed Fly Ash–Aluminum Coatings, *Mater. Des.*, 2010, **31**(3), p 1165–1173
14. A. Behera and S.C. Mishra, Application of Fly-Ash Composite in Plasma Surface Engineering, *National Seminar on Waste to Wealth Organized by Indian Institute of Metals-Bhubaneswar Chapter and SGAT-Bhubaneswar*, 14–15 December, 2012
15. J.R. Sunil, R. Keshawamurthy, C.P.S. Ramesh, and B.H. Channabasappa, Optimization of Process Parameters For Plasma Sprayed Flyash-Titania Composite Coatings, *Mater. Today Proc.*, 2015, **2**, p 2482–2490
16. A. Mateen, G.C. Saha, T.I. Khan, and F.A. Khalid, Tribological Behaviour of HVOF Sprayed Near-Nanostructured and Microstructured WC-17wt.% Co Coatings, *Surf. Coat. Technol.*, 2011, **206**(6), p 1077–1084
17. M. Doddamani, V.C. Shunmugasamy, N. Gupta, and H.B. Vijayakumar, Compressive and Flexural Properties of Functionally Graded Fly Ash Cenosphere–Epoxy Resin Syntactic Foams, *Polym. Compos.*, 2015, **36**(4), p 685–693
18. B.B. Kumar, M. Doddamani, S.E. Zeltmann, N. Gupta, M.R. Ramesh, and S. Ramakrishna, Processing of Cenosphere/HDPE Syntactic Foams Using an Industrial Scale Polymer Injection Molding Machine, *Mater. Des.*, 2016, **92**, p 414–423
19. S.E. Zeltmann, K.A. Prakash, M. Doddamani, and N. Gupta, Prediction of Modulus at Various Strain Rates from Dynamic Mechanical Analysis Data for Polymer Matrix Composites, *Compos. Part B*, 2017, **120**, p 27–34
20. V. Manakari, G. Parande, M. Doddamani, V.N. Gaitonde, I.G. Siddhalingshwar, V.C. Shunmugasamy, and N. Gupta, Dry Sliding Wear of Epoxy/Cenosphere Syntactic Foams, *Tribol. Int.*, 2015, **92**, p 425–438
21. B.B. Kumar, M. Doddamani, S.E. Zeltmann, N. Gupta, S. Gurupadu, and R.R.N. Sailaja, Effect of Particle Surface Treatment and Blending Method on Flexural Properties of Injection-Molded Cenosphere/HDPE Syntactic Foams, *J. Mater. Sci.*, 2016, **51**(8), p 3793–3805
22. S. Matthews, B. James, and M. Hyland, High Temperature Erosion of Cr<sub>3</sub>C<sub>2</sub>-NiCr Thermal Spray Coatings—The Role of Phase Microstructure, *Surf. Coat. Technol.*, 2009, **203**(9), p 1144–1153
23. J.K.N. Murthy, K.S. Prasad, K. Gopinath, and B. Venkataraman, Characterisation of HVOF Sprayed Cr<sub>3</sub>C<sub>2</sub>-50 (Ni20Cr) Coating and the Influence of Binder Properties on Solid Particle Erosion Behaviour, *Surf. Coat. Technol.*, 2010, **204**(24), p 3975–3985
24. S.C. Mishra, A. Satapathy, K.P. Singh, S. Sethy, P.V.A. Padmanabhan, K.P. Sreekumar, and R. Satpute, Plasma Spray Coating of Fly Ash on Metals for Tribological Application, in *Proceedings of the International Seminar on Mineral Processing Technology, Chennai*, 2006, p. 825–829
25. A.L. Robertson and K.W. White, Microscale Fracture Mechanisms of a Cr<sub>3</sub> C<sub>2</sub>-NiCr HVOF Coating, *Mater. Sci. Eng. A*, 2017, **688**, p 62–69
26. G. Bolelli, L.M. Berger, T. Börner, H. Koivuluo, V. Matikainen, L. Lusvardi, C. Lyphout, N. Markocsan, P. Nylén, P. Sassatelli, and R. Trache, Sliding and Abrasive Wear Behaviour of HVOF-and HVAF-Sprayed Cr<sub>3</sub> C<sub>2</sub>-NiCr Hardmetal Coatings, *Wear*, 2016, **358**, p 32–50
27. B.Q. Wang and Z.R. Shui, The hot Erosion Behavior of HVOF Chromium Carbide-Metal Cermet Coatings Sprayed with Different Powders, *Wear*, 2002, **253**(5), p 550–555
28. C.S. Ramachandran, V. Balasubramanian, and P.V. Ananthapadmanabhan, Erosion of Atmospheric Plasma Sprayed Rare Earth Oxide Coatings Under Air Suspended Corundum Particles, *Ceram. Int.*, 2013, **39**(1), p 649–672
29. H.S. Nithin, V. Desai, and M.R. Ramesh, Elevated Temperature Solid Particle Erosion Performance of Plasma-Sprayed Co-based Composite Coatings with Additions of Al<sub>2</sub> O<sub>3</sub> and CeO<sub>2</sub>, *J. Mater. Eng. Perform.*, 2017, **26**(11), p 5251–5261
30. G.C. Ji, C.J. Li, Y.Y. Wang, and W.Y. Li, Erosion Performance of HVOF-Sprayed Cr<sub>3</sub>C<sub>2</sub>-NiCr Coatings, *J. Therm. Spray Technol.*, 2007, **16**(4), p 557–565